# A multiresolution weather dataset for the Southwestern South Atlantic (2017-2018)

Luan C. V. Silva<sup>1</sup>, Lívia Sancho<sup>1</sup>, Mauricio S. Silva<sup>1</sup>, Elisa Passos<sup>3</sup>, Larissa F. R. Jacinto<sup>1</sup>, Rebeca S. Lyra<sup>1,2</sup>, Nilton O. Moraes<sup>1,2</sup>, Carina S. Bock<sup>1</sup>, Douglas M. Nehme<sup>1</sup>, Raquel Toste<sup>1</sup>, Jacques Honigbaum<sup>1</sup>, Rodrigo S. Luna<sup>1</sup>, Carlos H. Beisl<sup>4</sup>, Patricia M. Silva<sup>1</sup>, Adriano O. Vasconcelos<sup>1</sup>, Rian C. Ferreira<sup>1</sup>, Cédric Eneau<sup>5</sup>, Fernando A. Rochinha<sup>1</sup>, Luiz P. F. Assad<sup>1,2</sup>, Alvaro L. G. A. Coutinho<sup>1</sup>, Laura Bahiense<sup>1</sup>, and Alexandre G. Evsukoff<sup>1</sup>

- <sup>1</sup>COPPE, Universidade Federal do Rio de Janeiro
- <sup>2</sup>Instituto de Geociências IGEO, Universidade Federal do Rio de Janeiro
- <sup>3</sup> Faculdade de Oceanografia, Universidade do Estado do Rio de Janeiro
- <sup>4</sup>Geospatial Petroleum
- <sup>5</sup>TotalEnergies OneTech

## **ABSTRACT**

The Southwestern South Atlantic (SWSA) is a key region for climate research and renewable energy assessment, yet high-resolution meteorological data are scarce. We present a multiresolution dataset spanning February 2017âĂŞNovember 2018, combining Weather Research and Forecasting (WRF) simulations with Sentinel-1A/B Synthetic Aperture Radar (SAR) wind fields processed using the CMOD5 model. WRF outputs were generated every 30 minutes for three nested domains (9 km, 3 km, 1 km) through 975 short-term simulations. SAR/CMOD5 wind fields are provided at 500 m and 1 km resolution across 104 acquisition dates. Validation shows strong agreement: daily spatial averages of 10 m wind speed yield RMSE and MAE below 3 m/s on over 93% of acquisition days, while more than 91.5% of pixel-level residuals fall within Âś3 m/s. In situ measurements from the Itajaí buoy further confirmed the reliability of both sources. The dataset supports regional climate studies, wind energy resource assessment, and machine-learning applications in forecasting and downscaling, with usage examples included to aid practical adoption.

# 1 Background & Summary

The South Atlantic plays a pivotal role in the global climate system. It is the only ocean basin with a net equatorward heat transport, directly influencing heat redistribution, carbon storage, and global climate variability [1]. The limited understanding of local physical processes and climate variabilities in the Southwestern South Atlantic (SWSA) is largely attributed to sparse observational data and inaccuracies in long-term model integration [2].

Brazil is already among the world's largest producers of renewable electricity, with hydropower accounting for more than half of its electricity generation, leveraging the extensive river systems [3]. However, the region also has significant potential for other sources of large-scale renewable energy generation. The coastal area of Brazil has the potential for offshore wind energy estimated at  $\approx 3$  TW and more than 14,800 TWh of average annual electricity production [4, 5] and wave energy, with the potential to reduce  $CO_2$  emissions by approximately 44.52 million tons per year if gas-fired thermal energy is replaced [6]. According to Vinhoza & Schaeffer [7], few studies have comprehensively assessed Brazil's offshore potential, and those that exist have focused primarily on gross potential, often neglecting technological, environmental, and social constraints. While global models provide coverage of the region, increasing spatial resolution significantly enhances the representation of meteorological features such as wind variability and extreme events [8, 9].

Beyond improving our understanding of SWSA weather dynamics, a multiresolution weather dataset also provides rich training material for artificial intelligence (AI) methods. Owing to booming computing power, it is now possible to simulate climate systems at high resolution. This, combined with a surge in climate observations from weather satellites, creates a higher data volume that allows for the application of advanced machine learning methods to improve climate modelling and prediction [10]. However, data limitations are still recognized as a fundamental challenge in weather forecasting [11, 12]. AI can reduce both cost and time for delivering high-resolution weather data [13].

In this study, a dataset covering the southeastern coast of South America and the adjacent South Atlantic Ocean was created by integrating numerical simulations and satellite observations at multiple spatial resolutions. High-temporal-resolution

(30 min) outputs were generated by the Weather Research and Forecasting (WRF) model [14] through 975 independent runs-each lasting approximately 5.5 hours-for a combined computation time of approximately 5,362.5 hours. SAR images from Sentinel-1A/B C-band sensors [15, 16] were processed with the CMOD5 algorithm to estimate 10 m wind fields. Wind fields from the numerical and satellite models were validated against height-corrected in situ buoy measurements. This dataset spans February 2017 to November 2018 and provides exciting possibilities for AI applications, including forecast emulation [17, 18] and cross-scale downscaling [19]. The different data sources available allow observation-constrained bias correction [20, 21], and the wide range of weather variables allows multivariate analysis [22], leading to improved results and better exploitation of correlations among various atmospheric parameters.

#### 2 Methods

## 2.1 Study area

The study area is situated in the southwestern Atlantic, with a focus on the southern coast of Brazil and its adjacent offshore regions. To ensure adequate spatial coverage and resolution across the study region, a system of nested computational domains was constructed. The simulation used a one-way nesting strategy with three domains, as shown in Figure 1a. The outermost domain (D01), shown in blue, covers a broad area at a 9 km grid resolution; an intermediate domain (D02), in black, with a grid resolution of 3 km, is embedded within D01 and serves as a bridge by receiving input from D01 and passing boundary information to the innermost domain. The innermost domain (D03), shown in red, focuses on the core study area, which was configured with a grid resolution of 1 km (Figure 1a).

The area of the wind speed computed from the SAR acquisition frames overlapping the study area, serving as a reference for data validation along with the Itajaí meteo-oceanographic buoy location, are shown in Figure 1b. This combination of nested atmospheric domains and satellite coverage enables a detailed examination of wind variability from regional to local scales, with particular focus on the high-resolution D03 area.

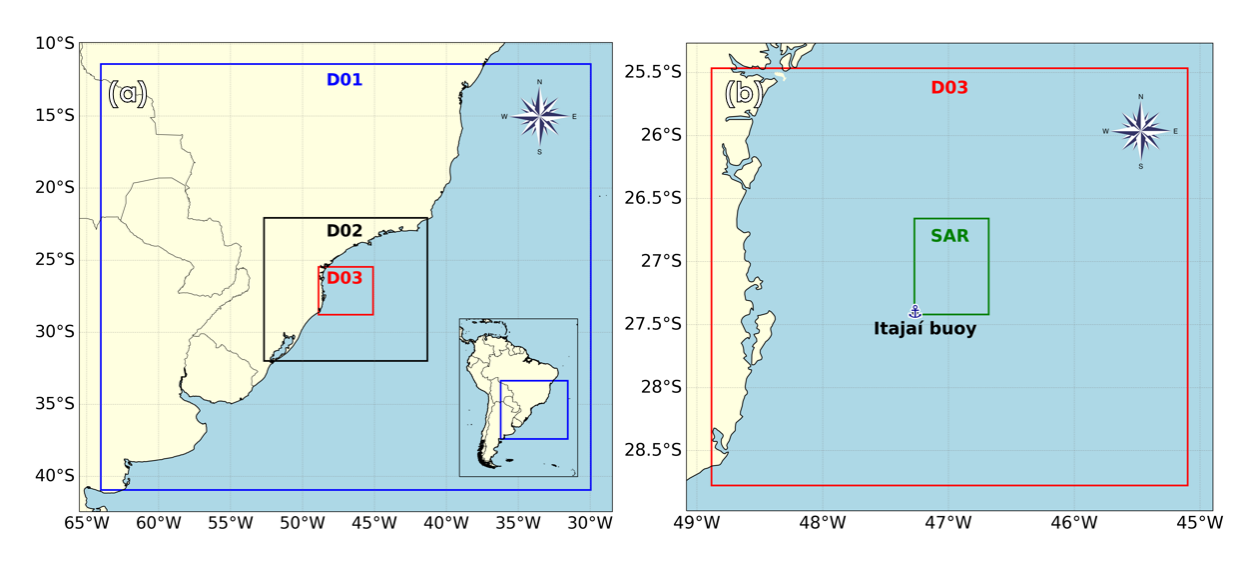


**Figure 1.** Study area. (a) Three-nested domains configured for the Weather Research and Forecasting model (WRF); D01 with 9 km resolution in blue, D02 with 3 km resolution in black, and D03 with 1 km resolution in red. (b) WRF model's most refined grid (D03), selected SAR region and the location of the Itajaí meteo-oceanographic buoy.

#### 2.2 The Weather Research and Forecasting (WRF) model

The atmospheric simulations were conducted using version 4.3.3 of the WRF model, which was configured with the Advanced Research WRF (ARW) dynamic core. This core integrates the full set of Navier-Stokes equations, thus avoiding the hydrostatic assumption and allowing for a detailed representation of atmospheric flows. Vertical discretization employs a terrain-following hybrid sigma-pressure coordinate. The model framework adopts the Arakawa staggered C-grid [23] and uses finite differences to solve the governing equations [24]. Staggered grids solve quantities in different regions of the grid, such as corners, centres, or faces, which means that dimensions can vary at one point depending on the variable. The mass, thermodynamic, scalar, and chemical variables are calculated in the centre of the grid cell. Moreover, the U and V components of the horizontal velocity are normal to the corresponding faces of the cell [14]. Thus, all dimensions with the suffix "stag" are located normal to the corresponding faces of the cell, while the others are located in the centre of the cell.

**Table 1.** WRF model configuration.

Description	Configuration	
Timing		
Simulation period	06:30h 06/02/2017 to 06h 18/11/2018	
Time step	48s	
Output Frequency	30 min	
Maps and grids		
Map projection	Mercator	
Horizontal grid spacing	9, 3 and 1 km (361 x 355)	
Grid Points	361 x 355 (all grids)	
Vertical levels	45	
Nesting strategy	One-way	
Topography data	GMTED2010 30 s (1 km) [25], GMTED2010 30 s (1 km) [25] and SRTM 9 s (90 m) [26]	
Land Use and Land Cover data	MODIS 30 s (1 km) [27], MODIS 30 s (1 km) [27], and MAPBIOMAS 30 m [28]	
Forcing strategy		
Initial and Boundary Conditions	FNL GFS (0.25 km) + SST from ROMS model on D03	
<b>Boundary Conditions Frequency</b>	6 hours	
Initialization	00 hour	
Runs duration	2 days + 6 hours (54 hours, 109 times)	
Spin-up time	6 hours	
Physical parametrization scheme	es	
Shortwave radiation	RRTMG [29]	
Longwave radiation	RRTMG [29]	
Cumulus parametrization	Multi-Scale Kain-Fritsch [30]	
Microphysics	Morrison Double-Moment [31]	
Surface Layer	Revised MM5 scheme for the surface layer [32]	
Land surface model	Noah-MP [33]	
Planetary boundary layer	Yonsei University (YSU) [34]	
Turbulence Diffusion Option	2	

As a consequence, the number of grid points for the "stag" variables is one unit greater than the other variables located in the centre of the cell grid. In this way, the variables XLAT and XLONG store the coordinate values located at the centers of the grid cells, whereas the variables XLAT\_U, XLONG\_U, XLAT\_V, and XLONG\_V store the coordinate values located at the respective faces of the grid cells. Detailed information can be found on the WRF website<sup>1</sup>.

Physical processes, including the radiation balance, microphysical processes, convection, turbulence, and surface interactions, are incorporated through parameterization schemes. In the vertical dimension, all the domains shared the same discretization, composed of 45 vertical levels distributed throughout the atmospheric column. Close to the surface, enhanced resolution was applied with four vertical levels approximately 200 metres above mean sea level, located at 26, 60, 103, and 160 metres, respectively. The nested domains were centred at 27.12°S and 46.99°W, using the Mercator projection. This positioning ensures dynamic consistency of the physical processes within the model and avoids inconsistencies or artificial relaxation effects at the boundaries of D03 relative to the core area of interest.

The physical options of the model were selected on the basis of previous evaluations and applications in similar contexts [35, 36, 37]. The chosen schemes are the following: the Morrison double moment scheme for cloud microphysics [31], the multiscale Kain–Fritsch scheme for convective processes [30], the rapid radiative transfer model for general circulation models (RRTMG) for both longwave and shortwave radiation [29], the Noah-MP scheme for land surface modelling [33], the revised Mesoscale Model (MM5) scheme for the surface layer [32], and the Yonsei University scheme for boundary layer dynamics [34]. Horizontal diffusion was treated in physical space to ensure better accuracy over complex terrain. The overall model configuration is displayed in Table 1.

Another important change in the data concerns the precipitation variables (RAINC and RAINNC). Originally, the precipitation data produced by WRF are cumulative over the entire duration of the one run (every 54 hours in the present case); however, the precipitation values made available are cumulative only between time intervals (30 minutes). Some variables can be derived indirectly from others, as shown in Table 2, which presents a relevant subset of such relationships.

The simulations utilized initial (IC) and boundary conditions (BC) from the final analysis (FNL) provided by the National

 $<sup>^{1}</sup> https://amps-backup.ucar.edu/information/configuration/wrf\_grid\_structure.html$ 

**Table 2.** Variables derived from WRF outputs and their formulas.

Variable	Formula
Atmospheric pressure $(P_{atm})$	P+PB
Geopotential height	PH + PHB
Height above mean sea level (z)	$\frac{PH + PHB}{g}$ , $g = 9.81 \text{m/s}^2$
Potential temperature $(\theta)$	T + 300
Air temperature $(T_{air})$	$\theta \left( \frac{P+PB}{100} \times \frac{1}{1000} \right)^{\frac{R}{c_p}},  \frac{R}{c_p} = 0.2854$

Centers for Environmental Prediction (NCEP), which were derived from the Global Forecast System (GFS2). This dataset offers global atmospheric fields with 0.25° horizontal resolution (approximately 24 km) and a temporal frequency of 6 hours. The GFS model has undergone continual development since the 1980s, with the most recent upgrade documented in 2021<sup>2</sup>. To improve the terrain representation in the boundary data, topographic information from the Shuttle Radar Topography Mission (SRTM) [26] and land cover data from the MapBiomas project [28] were incorporated. This approach follows the methodological refinements proposed in recent works [38, 39]. Additionally, to improve the air–sea interactions in the innermost domain (D03), sea surface temperature (SST) results from a hydrodynamic model were implemented. More details can be found in item 2.2. A summary of the main features of the simulations is presented in Table 1.

Sea surface temperature (SST) boundary condition. The hourly SST boundary conditions, with a horizontal resolution of ≈1 km, were obtained from a Regional Ocean Modelling System (ROMS) simulation. ROMS is a widely used three-dimensional free-surface hydrostatic model that solves primitive equations in a discretized space using an Arakawa C grid [40]. Hydrodynamic simulation was performed on a regional grid with 40 vertical layers and encompasses the region between 25.3°S and 28.9°S in latitude and 45.0°W and 49.0°W in longitude, i.e., including the D03 domain of the WRF model. The bathymetry was extracted from the Earth TOPOgraphy (ETOPO) 2022 [41] global model. The simulation was performed using the European Centre for Medium-Range Weather Forecasts (ECMWF) Reanalysis version 5 (ERA5) [42] as surface forcing and the daily results from the Copernicus Marine Environment Monitoring Service's GLORYS12V1 (Global Ocean Physics Reanalysis) product [43] as the IC and lateral BC. Astronomical tides from the TOPEX/Poseidon TPXO7.2 global model were also used as forcing at open boundaries [44, 45]. SST results were validated using the Operational Sea Surface Temperature and Ice Analysis dataset [46] and in situ data from the National Buoy Program (PNBOIA³) network.

## 2.3 Wind field estimation from synthetic aperture radar (SAR) images

**SAR imagery.** The wind field was estimated using data from the Sentinel-1A and Sentinel-1B satellites, provided free of charge through the European Space Agency (ESA) Sentinel portal<sup>4</sup>. The data were acquired in Interferometric Wide Swath (IW) mode, featuring a swath width of approximately 250 km and a spatial resolution of 5 m  $\times$  20 m (ESA, 2024). The original datasets are available at Level-1 processing in ground range detected (GRD) format, which consists of focused SAR data that have been detected, geocoded, and projected onto the ground range using the WGS84 ellipsoid model. The pixel values represent radar backscatter intensity in this format, with phase information discarded.

For the present study, a total of 104 SAR images were acquired over the offshore region of interest. The temporal availability of validated reference data from the Itajaí metoceanographic buoy guided image selection. Although the nominal temporal resolution of Sentinel-1 is 12 days per satellite, the combined coverage of Sentinel-1A and Sentinel-1B over the region of interest results in an effective revisit time of approximately 6 days for descending orbits. However, the image frames of the two satellites are spatially offset. Figure 1b illustrates the spatial configuration of the Sentinel-1A and Sentinel-1B acquisition frames. The Sentinel-1A frame is deliberately offset relative to the Sentinel-1B frame, enabling both enhanced temporal coverage and reduced imaging gaps.

The coverage area of the Sentinel-1A frame is approximately 44,558 km², while that of Sentinel-1B is about 52,660 km². The overlapping region between the two frames spans 32,500 km², corresponding to 73.0% and 61.7% of the Sentinel-1A and Sentinel-1B frames, respectively. Notably, the Itajaí metoceanographic buoy is located near the southern edge of the Sentinel-1A frame, whereas it is positioned closer to the of the Sentinel-1B frame. This spatial discrepancy may introduce edge effects in the wind field estimates derived from the Sentinel-1A data, potentially influencing comparisons with buoy measurements. To mitigate these effects and ensure consistency in the spatial analysis between the two acquisitions, a subset was defined on the basis of the intersection area between the Sentinel-1A and Sentinel-1B scenes (SAR layer in Figure 1b).

<sup>&</sup>lt;sup>2</sup>https://emc.ncep.noaa.gov/emc/pages/numerical\_forecast\_systems/gfs/documentation.php

<sup>&</sup>lt;sup>3</sup>https://www.marinha.mil.br/chm/dados-do-goos-brasil/pnboia

<sup>&</sup>lt;sup>4</sup>https://dataspace.copernicus.eu/explore-data/data-collections/sentinel-data

This subset focuses on the central portion of the overlapping region and includes the buoy location, thereby reducing spatial mismatches and allowing for a more robust comparison of wind estimates across sensors.

In SAR imagery, ships appear as strong backscatter and are represented as bright targets against the ocean surface (Figure 2). Masking these high-reflectivity objects prevents such targets from introducing artefacts into the wind speed retrieval process. Without this masking step, ship signatures may lead to erroneous wind speed estimates, manifesting as outliers in the derived wind field.

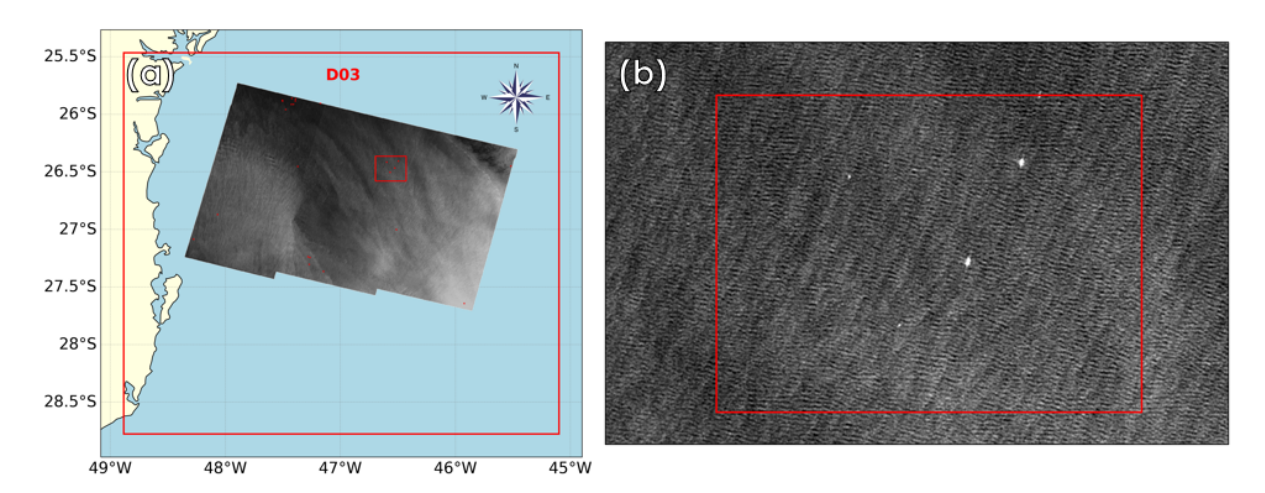


**Figure 2.** (a) Bright object detection mask produced by the SNAP platform, highlighting potential ship targets; (b) detailed view of the corresponding objects identified in the SAR image.

A series of specific functions was developed to detect and mask anomalous reflectors, thereby mitigating this issue. Ship detection is based on identifying point-like intensity peaks that significantly exceed the surrounding pixel values. In contrast, oil slick detection focuses on regions with anomalously low backscatter intensities.

The primary function implemented for this purpose, named  $ship\_detection$ , is designed to identify both types of anomalies. By default, pixels with values above the  $99.7^{th}$  percentile of the image intensity distribution are classified as ships, whereas pixels below the  $0.01^{st}$  percentile are flagged as potential oil slicks. These threshold values are configurable and can be adapted to suit specific application requirements.

Following anomaly detection, the *dilation\_mask* function is applied to expand the initially identified pixel regions. This dilation step is crucial for eliminating discontinuities and forming cohesive, contiguous masks. The operation uses a default square structuring element of  $3 \times 3$  pixels, although this parameter can be adjusted depending on the desired level of mask expansion.

To reconstruct the masked regions in the SAR images, we employed an image inpainting function, a technique commonly used for restoring degraded or missing areas in digital images, such as damaged photographs. This function provides two available methods: terrain elevation-dependent attenuation (TELEA) and the Navier–Stokes method. The TELEA method uses the fast marching method to propagate known pixel values into the masked regions iteratively [47]. On the other hand, the Navier–Stokes method applies partial differential equations grounded in fluid dynamics to guide the reconstruction process [48]. A comparative analysis was conducted to evaluate the performance of both techniques within the context of wind field estimation from SAR images. The Navier–Stokes method was selected as the default approach because of its superior performance in maintaining image continuity and minimizing edge artefacts. Nevertheless, the inpainting method remains a configurable parameter within the implementation, allowing users to adapt the choice according to specific application requirements.

**The CMOD5 geophysical model.** The subsequent stage of the methodology involves applying the CMOD5 geophysical model function (GMF), developed by Hersbach in 2003 [49]. This empirical model is designed to estimate the near-surface wind speed and direction from the normalized radar cross-section (NRCS or  $\sigma^0$ ) obtained from C-band SAR measurements.

As wind interacts with the ocean surface, it generates small-scale roughness patterns that tend to align with the wind direction. These surface features modulate the radar backscatter signal, a relationship well documented in the literature (e.g., Wackerman et al. [50]). The CMOD5 model captures this relationship by expressing  $\sigma^0$  as a function of three key variables: wind speed at 10 m above sea level ( $u_{10}$ , in m/s), the relative angle between the radar look direction and wind direction ( $\Phi$ , in degrees), and the local incidence angle of the radar beam ( $\theta$ , in degrees). Formally, the model is expressed as  $\sigma^0 = f(u_{10}, \Phi, \theta)$ , where f is a nonlinear empirical function calibrated using extensive datasets from scatterometers, SAR observations, buoys, and numerical weather prediction models.

The wind direction is first estimated using the u and v components of the wind vectors provided by the WRF model. These components are interpolated to match the spatial resolution defined for the SAR-based analysis. The wind direction is computed for each grid cell and subsequently compared with the direction retrieved from SAR imagery using the CMOD5 model. The wind speed field is derived by applying the CMOD5 geophysical model to the Sentinel-1 SAR data. This process yields two wind speed products: one derived from the WRF model and the other obtained directly from the SAR imagery through inversion of the CMOD5 function.

#### 3 Data records

The dataset acquired in this data descriptor is available at the Harvard Dataverse<sup>5</sup>. The dataset is composed of: (1) WRF model outputs with selected variables (Table 4), (2) SAR/CMOD5 wind spatial retrievals, (3) in situ buoy data (single location). Table 3 shows the grid sizes of in the dataset for WRF and SAR/CMOD5 layers for the available spatial resolutions. Note that the WRF grid dimensions listed in Table 3 refer to the number of mass-point (C-grid) locations in the horizontal (X-Y) plane-that is, the unstaggered model grid. These values represent the size of a single horizontal slice of mass centres in the WRF output.

**Table 3.** Grid dimensions for WRF and SAR/CMOD5 10 m wind speed data at different spatial resolutions.

Resolution	WRF	SAR/CMOD5
500 m	_	164 × 114
1 km	$354 \times 360$	$82 \times 57$
3 km	$354 \times 360$	_
9 km	$354 \times 360$	_

WRF data The WRF output is provided for three nested domains (D01, D02, and D03) spanning from 00:30 UTC 06 February 2017 through 06 UTC 18 November 2018 at 30-minute temporal resolution. Table 4 lists the WRF variables in the dataset. The first seven are coordinates, while the rest are data variables. For more details, refer to the WRF Users' Guide<sup>6</sup>. The WRF outputs were stored as daily NetCDF (.nc) files, with each file reaching approximately 480 GB. Separate files are available for each model grid, and all variables are stored together with their corresponding coordinates.

WRF output is provided for three nested domains (D01, D02, D03) spanning from 00:30 UTC 06 February 2017 through 06 UTC 18 November 2018 at 30-minute temporal resolution. Table 4 lists the WRF variables in the dataset. The first seven are coordinates, while the rest are data variables. For more details, refer to the WRF Users' Guide<sup>7</sup>. The WRF outputs were stored as daily NetCDF (.nc) files, with each file reaching approximately 480 GB. Separate files are available for each model grid, and all variables are stored together with their corresponding coordinates.

Bilgili et al. (2022) reported that the 2020 mean hub height of offshore wind turbines was 104.03 m [51]. Figure 3 shows the corresponding heights at a range of vertical levels, calculated using the formula given in Table 2, with the highest levels exceeding 2,000 m. However, the full set of "4D" variables required to represent every model level produces very large files. Many climate-related applications, such as assessments of offshore wind-energy potential, do not require high altitudes. Accordingly, we limit this dataset to the first 6 staggered and 5 centred vertical layers, substantially reducing the file size. The data with all layers are available upon request.

<sup>&</sup>lt;sup>5</sup>https://dataverse.harvard.edu/dataset.xhtml?persistentId=doi:10.7910/DVN/OUEZ0H

<sup>&</sup>lt;sup>6</sup>https://www2.mmm.ucar.edu/wrf/users/docs/user\_guide\_v4/contents.html

<sup>&</sup>lt;sup>7</sup>https://www2.mmm.ucar.edu/wrf/users/docs/user\_guide\_v4/contents.html

**Table 4.** Description of WRF output variables available in the dataset.

Variable	Description and units	Dimensions
Times	Reference date (calendar date)	1D (Time)
XLAT	Latitude values of grid cell centre points (degree_north)	2D (south_north, west_east)
XLONG	Longitude values of grid cell centre points (degree_east)	2D (south_north, west_east)
XLAT_U	Latitude values of grid cell zonal faces (degree_north)	2D (south_north, west_east_stag)
XLONG_U	Longitude values of grid cell zonal faces (degree_east)	2D (south_north, west_east_stag)
XLAT_V	Latitude values of grid cell meridional faces (degree_north)	2D (south_north_stag, west_east)
XLONG_V	Longitude values of grid cell meridional faces (degree_east)	2D (south_north_stag, west_east)
LU_INDEX	Land use index (categorical)	2D (south_north, west_east)
HGT	Terrain height above sea level (m)	2D (south_north, west_east)
LANDMASK	Land-sea mask $(1 = land, 0 = water)$	2D (south_north, west_east)
ZNU	Vertical coordinate at full (mass) levels (m)	2D (Time, bottom_top)
ZNW	Vertical coordinate at half (staggered) levels (m)	2D (Time, bottom_top_stag)
T2	2 m air temperature (K)	3D (Time, south_north, west_east)
TH2	2 m potential temperature (K)	3D (Time, south_north, west_east)
SST	Sea surface temperature (K)	3D (Time, south_north, west_east)
PHB	Base-state geopotential $(m^2 \cdot s^{-2})$	3D (bottom_top_stag, south_north, west_east)
PB	Base-state pressure (Pa)	3D (bottom_top, south_north, west_east)
PSFC	Surface pressure (Pa)	3D (Time, south_north, west_east)
RAINC	Cumulative convective precipitation (kg⋅m <sup>-2</sup> )	3D (Time, south_north, west_east)
RAINNC	Cumulative non-convective precipitation (kg⋅m <sup>-2</sup> )	3D (Time, south_north, west_east)
U10	10 m U-component of wind (m⋅s <sup>-1</sup> )	3D (Time, south_north, west_east)
V10	10 m V-component of wind (m·s <sup>-1</sup> )	3D (Time, south_north, west_east)
T	Perturbation potential temperature (K)	4D (Time, bottom_top, south_north, west_east)
PH	Perturbation geopotential (m <sup>2</sup> ·s <sup>-2</sup> )	4D (Time, bottom_top_stag, south_north, west_east)
P	Perturbation pressure (Pa)	4D (Time, bottom_top, south_north, west_east)
U	U-component of wind (m·s <sup>-1</sup> )	4D (Time, bottom_top, south_north, west_east_stag)
V	V-component of wind (m·s <sup>-1</sup> )	4D (Time, bottom_top, south_north_stag, west_east)
W	Vertical velocity (m⋅s <sup>-1</sup> )	4D (Time, bottom_top_stag, south_north, west_east)

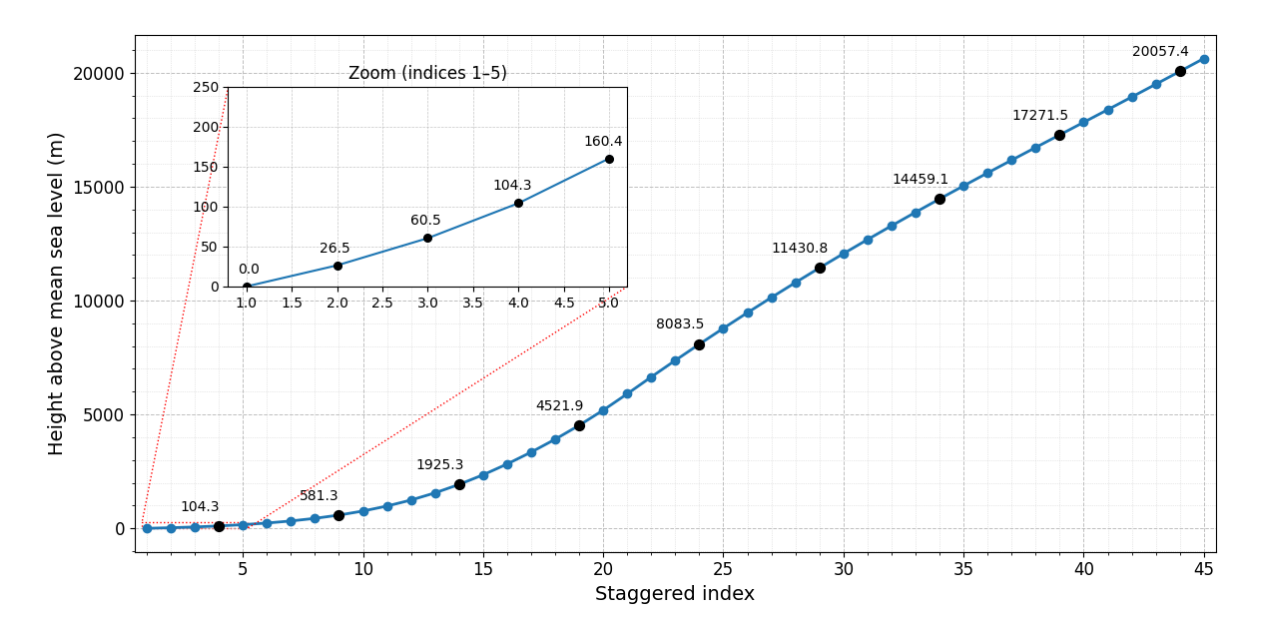


**Figure 3.** Approximate (pressure-dependent) height above mean sea level for each WRF-staggered vertical index, computed as (PH + PHB)/g, where PH and PHB are are the perturbation and base-state geopotential respectively, and g is the gravitational acceleration.

As an illustrative case, Figures 4 and 5 present the near-surface meteorological fields simulated across the three model

domains for the experiment initialized on August 1<sup>st</sup>, 2017. These figures specifically depict the spatial distribution of 2-metre air temperature and 10-metre wind.

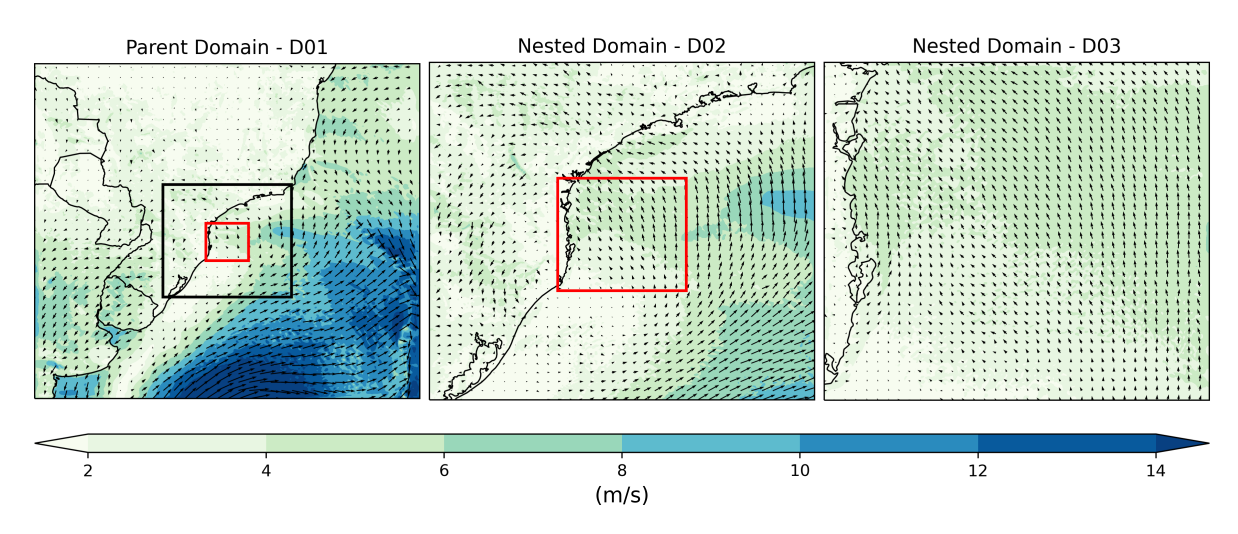


**Figure 4.** Maps of the wind fields at 10 m from the 9km (D01), 3km (D02) and 1 km (D03) grids of the August 1<sup>st</sup>, 2017 run of the WRF model.

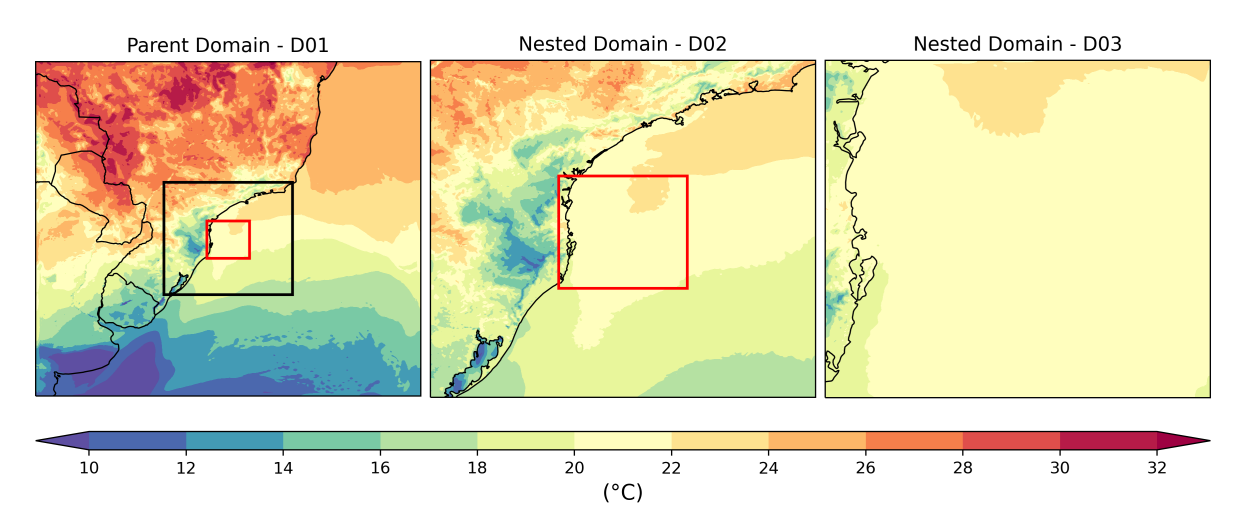


**Figure 5.** Maps of 2-metre temperature fields from the 9 km (D01), 3 km (D02) and 1 km (D03) grids of the August 1<sup>st</sup>, 2017, run of the WRF model.

**SAR/CMOD5 data** All the processed SAR/CMOD5 data are consolidated into a single NetCDF file containing 104 acquisition dates between 07 February 2017 and 11 November 2018. SAR-derived wind fields computed via CMOD5 inversion after masking and inpainting. The variables present in the SAR/CMOD5 data are shown in Table 5. Two data files were created on the basis of spatial resolution (Table 6). Examples of the wind speed fields derived from the model at both resolutions are shown in Figure 6.

**Table 5.** Description of SAR/CMOD5 variables available in the dataset.

Variable	Description and units	Dimensions
Times	Date of SAR image acquisition (calendar date)	1D (Time)
XLAT	Latitude values (degree_north)	2D (south_north, west_east)
XLONG	Longitude values (degree_east)	2D (south_north, west_east)
XSAT	Satellite identifier	1D (satellite)
U10	10 m U-component of wind (m·s <sup>-1</sup> )	3D (Time, south_north, west_east)
V10	10 m V-component of wind (m⋅s <sup>-1</sup> )	3D (Time, south_north, west_east)
WIND_SPD	Wind speed magnitude (m·s <sup>-1</sup> )	3D (Time, south_north, west_east)
WIND_DIR	Wind direction (degrees from north)	3D (Time, south_north, west_east)

**Table 6.** Summary of SAR/CMOD5 NetCDF files.

File Name	Size	Description
data_SAR_500m.nc	7.47 MB	SAR/CMOD5 wind speed fields at 500 m spatial resolution.
data_SAR_1000m.nc	29.83 MB	SAR/CMOD5 wind speed fields at 1-km spatial resolution.

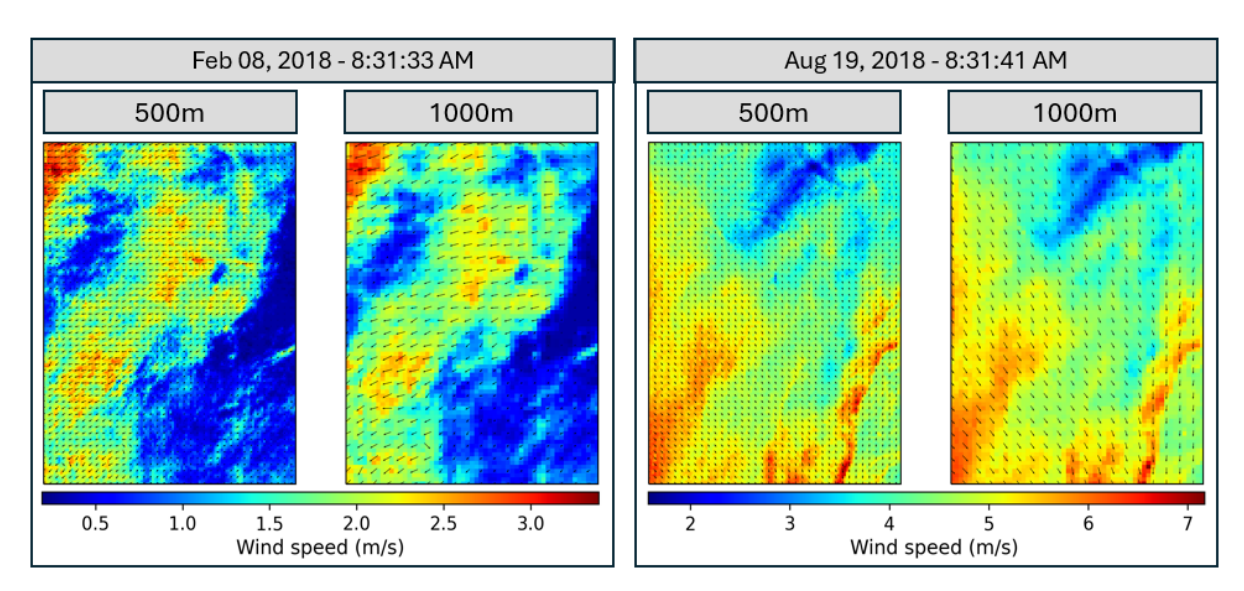


**Figure 6.** SAR/CMOD5 Wind speed field maps derived from the SAR images of February 8, 2018, and August 19, 2018, at 500 m and 1 km spatial resolution.

**Itajaí oceanographic buoy** In situ observations from the Itajaí metoceanographic buoy (PNBOIA program) are also used to evaluate the consistency of these results. The observations include date, time, geographic coordinates, wind speed, and wind direction. However, the observations are at a height of approximately 4 m. To compare them to the 10-m wind fields available in the WRF and SAR/CMOD5 outputs, we used the logarithmic profile law (Equation 1) [52]:

$$u(z) = u(z_{\text{ref}}) \frac{\ln(\frac{z}{z_0})}{\ln(\frac{z_{\text{ref}}}{z_0})}.$$
 (1)

where z is the target height for wind speed estimation [m],  $z_{\text{ref}}$  is the reference height at which the speed  $u(z_{\text{ref}})$  was measured [m], u(z) is the wind speed at height z [m/s], and  $z_0$  is the surface roughness length [m]. The surface roughness length was estimated following the ERA5 methodology [42]. Given the relevance of the buoy data for the region-located within the WRF and SAR/CMOD5 study areas, these measurements are also provided in tabular format, with one row per observation time. The data is stored in the file itajai\_buoy.csv (2.17 MB), and the variables (columns) are listed in Table 7.

**Table 7.** Description of buoy variables available in the dataset.

Variable	Description and units
Time	Date and time of observation
Latitude	Latitude position of buoy (degree_north)
Longitude	Longitude position of buoy (degree_east)
Wdir	Wind direction (degrees from north)
Wspd	Wind speed $(m \cdot s^{-1})$
Fsr	Surface roughness length [m]
Wspd_10	Wind speed adjusted to 10 m height (m·s <sup>-1</sup> )
is_SAR	SAR comparison flag (Subsection 4.2)

## 4 Technical Validation

The data products presented in this dataset were evaluated using two approaches over the full observation period. First, we compared the 10-metre wind fields from the WRF model and the SAR/CMOD5 retrievals. Afterwards, we validated both datasets using in situ wind measurements from the Itajaí oceanographic buoy by comparing them with the nearest grid points in the WRF and SAR/CMOD5 data.

## 4.1 WRF and SAR/CMOD5 grid comparison

The wind speed data produced by the innermost WRF numerical model domain were compared with the results obtained by the SAR/CMOD5 model on the days/hours of image acquisition. Two different approaches were used for validation: a global analysis of the grid points and an analysis of the temporal mean. The 1-km SAR data and D03 WRF domain were used. Because both have the same spatial resolution and SAR/CMOD5 interpolated values to match the WRF grid, we have  $82 \times 57$  values at each time (Table 3) and 104 available SAR images. Therefore, there is a total of N = 486,096 records.

**Global analysis.** For comparison, the WRF model outputs corresponding to the times closest to the SAR image acquisitions were used. The SAR images analysed in this study were acquired between 08:31:26 and 08:32:14 UTC (HH:MM:SS). Because the WRF model provides outputs at 30-minute intervals (i.e., at 00:00 and 30:00 UTC each hour), the 08:30:00 UTC output on the respective acquisition days was selected for comparison. Table 8 shows that the mean residual between the SAR/CMOD5 and WRF results (SAR/CMOD5 - WRF) is low (0.145 m/s), and the  $5^{th}$  and  $95^{th}$  percentiles indicate that 90% of the residuals lie within the range [-3.297, 2.366], reflecting overall agreement between the datasets. However, the standard deviation of the residuals (1.782 m/s) suggests notable local discrepancies.

**Table 8.** Statistics of the WRF, SAR/CMOD5 data and their difference

	WRF	SAR/CMOD5	Residuals
Minimum	0.080	0.200	-10.635
Maximum	16.806	19.775	11.541
Mean	6.719	6.506	-0.213
Standard deviation	2.813	2.687	1.782
1 <sup>st</sup> percentile	1.334	0.580	-5.022
5 <sup>th</sup> percentile	2.246	2.427	-3.297
95 <sup>th</sup> percentile	11.380	11.349	2.366
99 <sup>th</sup> percentile	14.324	14.104	3.647

The distributions are shown in Figure 7. The distributions of the wind intensity values in each pixel for the WRF and SAR/CMOD5 models are shown in Figure 7a. The distributions are shown in Figure 7. The relative frequency distributions of the wind speed values (per pixel) for both the WRF and the SAR/CMOD5 data are shown in Figure 7a. The distributions exhibit similar overall patterns, with the highest frequencies occurring in the [4-6) and [6-8) m/s intervals for both models. SAR/CMOD5 has a heavier right tail, whereas WRF has greater values in the lower range ([0-4) m/s), which is consistent with the results in Table 8.

The cumulative distributions of the absolute residuals between the SAR/CMOD5 and WRF models are shown in Figure 7b. More than 90% of the absolute residuals are below 3 m/s, indicating good agreement between the distributions. This is supported by the error metrics [53], with an RMSE (Eq. 2) of 1.795 m/s and an MAE (Eq. 3) of 1.388 m/s.

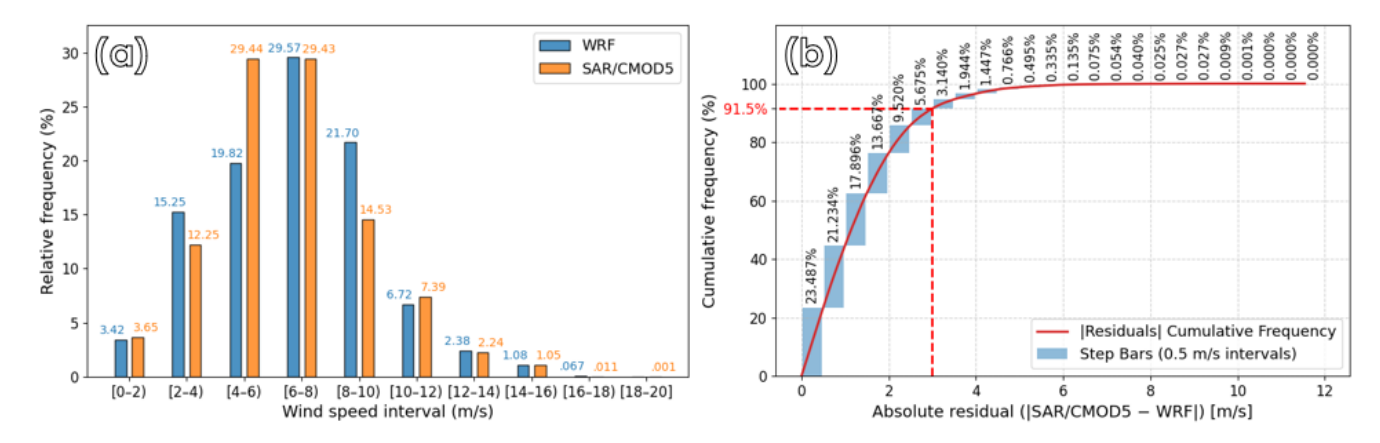


**Figure 7.** (a) Comparison of 10-m wind speed data from WRF and SAR/CMOD5 at the times of SAR image acquisition. (a) Relative frequency distributions of average wind speeds for the WRF (blue) and SAR/CMOD5 (orange) data across 2 m/s intervals. (b) Cumulative distribution of absolute residuals, including a step-bar representation of the incremental contributions within 0.5 m/s bins and the cumulative frequency curve.

root mean squared error (RMSE) = 
$$\sqrt{\frac{1}{N} \sum_{t=1}^{N} residual(t)^2}$$
 (2)

mean absolute error (MAE) = 
$$\frac{1}{N} \sum_{t=1}^{N} \left| redisual(t) \right|$$
 (3)

**Temporal mean.** In the second approach, the WRF and SAR/CMOD5 wind speeds were compared on the basis of the daily mean across all pixels ( $82 \times 57 = 4674$ ) within the region. The upper panel of Figure 8 presents the daily mean wind speeds from both models over the 104 SAR acquisition days, while the lower panel displays the corresponding daily error metrics. As shown in the figure and summarized in Table 9, at the stricter 1 m/s threshold, over one-third of the days (35.6%) have MAE values within the limit, whereas only 21.2% meet this criterion for the RMSE. This indicates stronger local deviations that significantly affect the RMSE, which is more sensitive to outliers. Nonetheless, more than 93% of the days exhibit RMSE and MAE values less than 3 m/s. Overall, the results indicate good agreement between the models in terms of daily spatial averages.

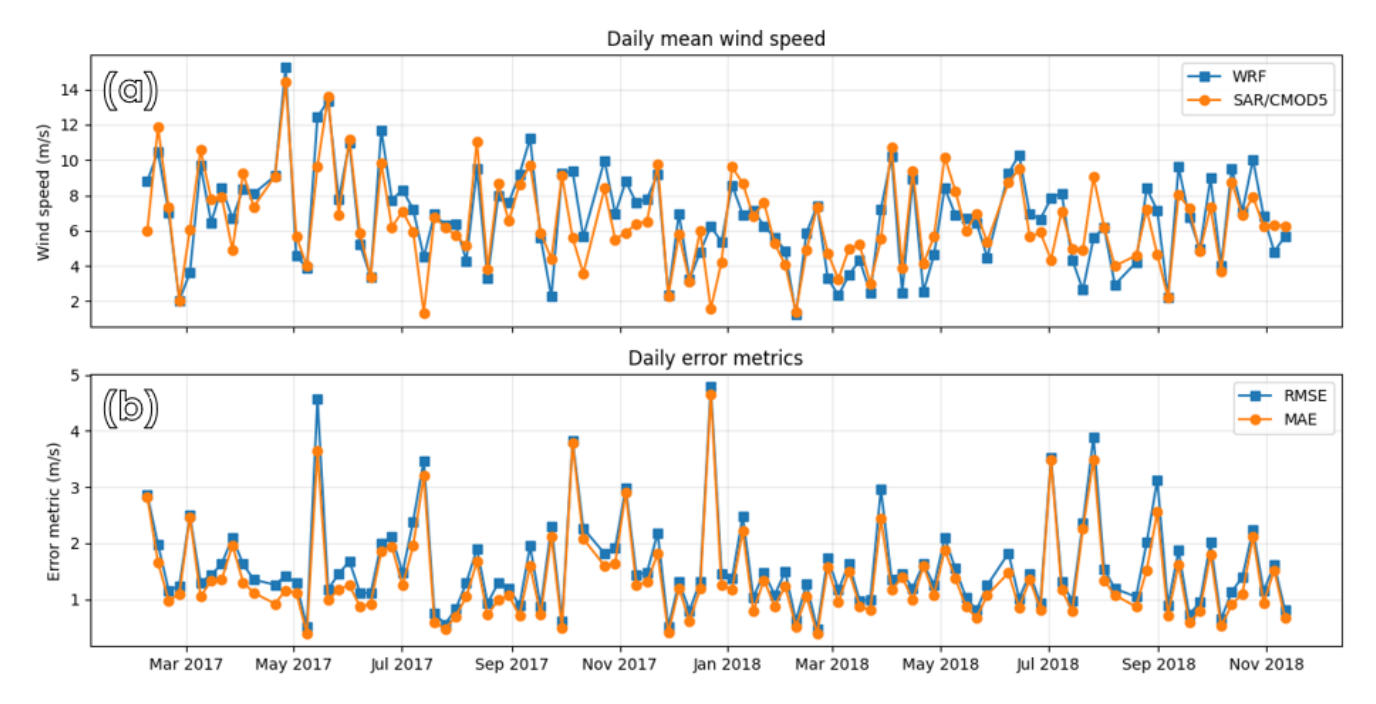


**Figure 8.** Daily mean wind speed at 10 m (m/s) from the WRF and SAR/CMOD5 models over 104 SAR acquisitions spaced at 6-day intervals between February 2017 and November 2018. The upper panel shows the time series of daily spatial averages from both models. The lower panel presents the corresponding RMSE and MAE for each day.

**Table 9.** Proportion of days used in the comparison with RMSE and MAE below given thresholds.

Threshold (m/s)	$RMSE \leq Threshold$	$\mathbf{MAE} \leq \mathbf{Threshold}$
1	22/104 (21.2%)	37/104 (35.6%)
2	81/104 (77.9%)	88/104 (84.6%)
3	97/104 (93.3%)	98/104 (94.2%)
5	104/104 (100.0%)	104/104 (100.0%)

## 4.2 Buoy comparison

To evaluate the accuracy of the WRF model and SAR/CMOD5 wind speed estimates, we compare them with measurements from the Itajaí buoy. The buoy coordinates vary slightly over time, but for consistency, we used a fixed position of 27°24.35'S, 47°15.93'W. The wind speed values from the buoy were adjusted to represent the 10-metre height.

WRF The WRF simulation data spans from 2017-02-06 06:30 UTC to 2018-11-18 06:00 UTC. Buoy observations are recorded hourly at hh:00:00 UTC. Within the entire WRF simulation period, there are 59 missing records in the buoy dataset: one isolated missing hour on 2018-04-15 at 14:00 UTC and one continuous gap of 58 hours from 2018-04-30 at 01:00 UTC to 2018-05-02 at 10:00 UTC (inclusive). After accounting for these gaps, there are 15,497 timestamps with overlapping WRF and buoy wind speed data. Because the closest grid point in the WRF data was used for comparison, 15,497 is also the number of observations used in the comparison.

The wind speed distributions from the WRF model and the Itajaí buoy are compared in Figure 9. Panel (a) shows the relative frequency of the wind speed values binned at 2 m/s intervals, revealing distinct distributions—most notably, a heavier right tail in the buoy data. Despite these differences, the cumulative distribution of absolute residuals in panel (b) indicates that more than 80% of the absolute residuals fall below 3 m/s. The calculated RMSE and MAE are 2.538 m/s and 1.956 m/s, respectively.

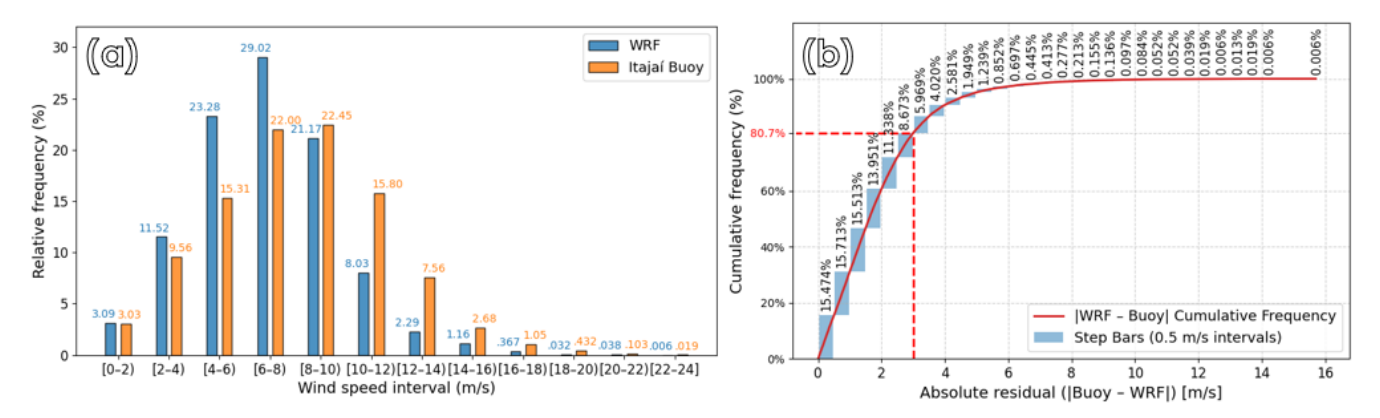


**Figure 9.** (a) Comparison of 10 m wind speed data from WRF and SAR/CMOD5 at the times of SAR image acquisition. (a) Relative frequency distributions of average wind speeds for WRF (blue) and Itajaí buoy (orange) data across 2 m/s intervals. (b) Cumulative distribution of absolute residuals, including a step-bar representation of the incremental contributions within 0.5 m/s bins and the cumulative frequency curve.

**SAR/CMOD5** The buoy provides hourly observations (hh:00:00), and because the SAR acquisitions during the study period occurred between 08:31:26 and 08:32:14 UTC, the closest hourly record at 09:00 UTC was used for comparison. Similarly, the nearest grid point in the SAR data was selected. The good agreement between the SAR-derived wind speeds and the buoy observations across the entire time series of 104 SAR acquisitions spaced at 6-day intervals is shown in Figure 10. An MAE of 1.57 m/s and a RMSE of 2.03 m/s support these results, with a higher RMSE reflecting the influence of larger individual deviations between the SAR and buoy measurements.

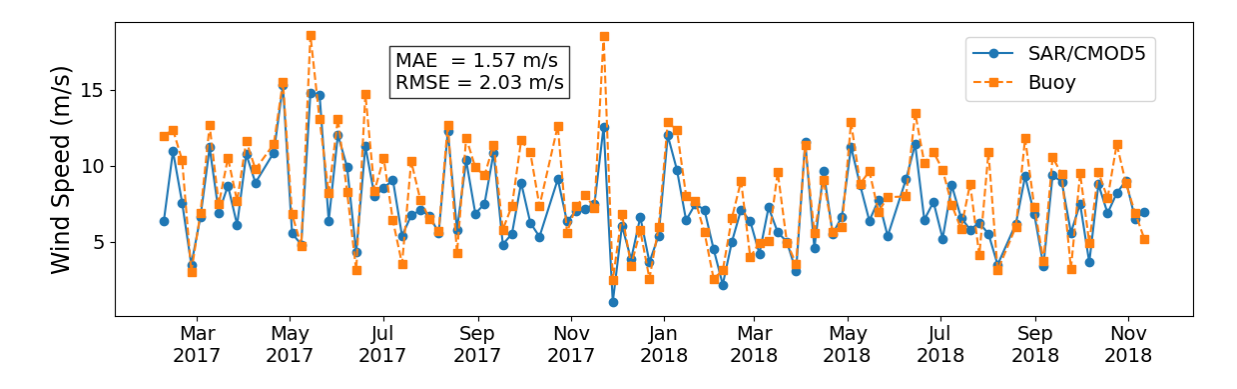


**Figure 10.** Time series of wind speed (m/s) from the SAR/CMOD5 closest grid point to the Itajaí buoy and buoy measurements adjusted to a height of 10 metres. The plot includes 104 SAR acquisitions at 6-day intervals between February 2017 and November 2018.

## 5 Usage notes

The dataset files are provided in NetCDF (.nc) format, a widely used standard for array-oriented scientific data. This format allows for easy manipulation and analysis using libraries such as xarray in Python. To work with the dataset, you can load a file named "filename.nc" using the following code snippet:

```
import xarray as xr
dataset = xr.open_dataset("data_D01_20170206.nc")
u_wind_component = dataset["U"]
```

The code behind Section 4, along with example scripts demonstrating key workflows (e.g., loading WRF output, computing heights, and generating figures), is available on GitHub (https://github.com/luancvieira/Southwestern-South-Atlantic-weather-dataset).

## Data availability

The dataset is accessible in the Harvard Dataverse repository: https://dataverse.harvard.edu/dataset.xhtml?persistentId=doi:10.7910/DVN/OUEZOH. The data with all 45 vertical layers is available upon request.

# Code availability

The dataset was produced using the Weather Research and Forecasting (WRF) model, which is accessible via its Git repository (https://github.com/wrf-model/WRF). Further information can be obtained from the official website of the model (https://www2.mmm.ucar.edu/wrf/users). SAR data processing relied on the XSAR (https://github.com/umr-lops/xsar/tree/develop) and XSARSEA (https://github.com/umr-lops/xsarsea) Python libraries, which offer tools for reading, processing, and analyzing Sentinel-1 SAR measurements for ocean and coastal applications.

## References

- **1.** Chidichimo, M. P. *et al.* Energetic overturning flows, dynamic interocean exchanges, and ocean warming observed in the south atlantic. *Communications Earth & Environment* **4**, 10 (2023).
- **2.** Gramcianinov, C. B. *et al.* Recent changes in extreme wave events in the south-western south atlantic. *State of the Planet* **1**, 1–12 (2023).
- **3.** Catolico, A. C. C., Maestrini, M., Strauch, J. C. M., Giusti, F. & Hunt, J. Socioeconomic impacts of large hydroelectric power plants in brazil: A synthetic control assessment of estreito hydropower plant. *Renewable and Sustainable Energy Reviews* **151**, 111508 (2021).
- **4.** Azevedo, S. S. P. d., Junior, A. O. P., Silva, N. F. d., Araújo, R. S. B. d. & Júnior, A. A. C. Assessment of offshore wind power potential along the brazilian coast. *Energies* **13**, 2557 (2020).
- **5.** González, M. O. A., Santiso, A. M., de Melo, D. C. & de Vasconcelos, R. M. Regulation for offshore wind power development in brazil. *Energy Policy* **145**, 111756 (2020).
- **6.** Bastos, A. S., Souza, T. R. C. d., Ribeiro, D. S., Melo, M. d. L. N. M. & Martinez, C. B. Wave energy generation in brazil: A georeferenced oscillating water column inventory. *Energies* **16**, 3409 (2023).
- 7. Vinhoza, A. & Schaeffer, R. Brazil's offshore wind energy potential assessment based on a spatial multi-criteria decision analysis. *Renewable and Sustainable Energy Reviews* **146**, 111185 (2021).
- **8.** Hadjipetrou, S. & Kyriakidis, P. High-resolution wind speed estimates for the eastern mediterranean basin: A statistical comparison against coastal meteorological observations. *Wind* **4**, 311–341 (2024).
- **9.** Ryu, J., Kim, H., Wang, S.-Y. S. & Yoon, J.-H. Increasing resolution and accuracy in sub-seasonal forecasting through 3d u-net: the western us. *EGUsphere* **2025**, 1–18 (2025).
- 10. Bracco, A. et al. Machine learning for the physics of climate. Nature Reviews Physics 7, 6–20 (2025).
- **11.** Pagano, T. C. *et al.* Challenges of operational weather forecast verification and evaluation. *Bulletin of the American Meteorological Society* **105**, E789–E802 (2024).

- **12.** Chen, L. *et al.* Machine learning methods in weather and climate applications: A survey. *Applied Sciences* **13**, 12019 (2023).
- **13.** Wu, Y. & Xue, W. Data-driven weather forecasting and climate modeling from the perspective of development. *Atmosphere* **15**, 689 (2024).
- **14.** Skamarock, W. C. e. a. A description of the advanced research wrf model version 4.3. Tech. Rep., NCAR (2021). 10.5065/1dfh-6p97.
- **15.** Hadjipetrou, S. *et al.* Evaluating the suitability of sentinel-1 sar data for offshore wind resource assessment around cyprus. *Renewable Energy* **182**, 1228–1239 (2022).
- **16.** Moreira, A. *et al.* A tutorial on synthetic aperture radar. *IEEE Geoscience and Remote Sensing Magazine* **1**, 6–43, 10.1109/MGRS.2013.2248301 (2013).
- **17.** Li, L., Carver, R., Lopez-Gomez, I., Sha, F. & Anderson, J. Generative emulation of weather forecast ensembles with diffusion models. *Science Advances* **10**, eadk4489 (2024).
- **18.** Wang, J., Balaprakash, P. & Kotamarthi, R. Fast domain-aware neural network emulation of a planetary boundary layer parameterization in a numerical weather forecast model. *Geoscientific Model Development* **12**, 4261–4274 (2019).
- **19.** Oh, M., Lee, J., Kim, J.-Y. & Kim, H.-G. Machine learning-based statistical downscaling of wind resource maps using multi-resolution topographical data. *Wind Energy* **25**, 1121–1141 (2022).
- **20.** Zhang, J., Gao, Z. & Li, Y. Deep-learning correction methods for weather research and forecasting (wrf) model precipitation forecasting: a case study over zhengzhou, china. *Atmosphere* **15**, 631 (2024).
- **21.** Wang, F. & Tian, D. On deep learning-based bias correction and downscaling of multiple climate models simulations. *Climate Dynamics* **59**, 3451–3468 (2022).
- **22.** Zhu, X. *et al.* Weather2k: A multivariate spatio-temporal benchmark dataset for meteorological forecasting based on real-time observation data from ground weather stations. *arXiv preprint arXiv:2302.10493* (2023).
- **23.** Mesinger, F. & Arakawa, A. Numerical methods used in atmospheric model, volume 1. Tech. Rep., International Council of Scientific Unions-World Meteorological Organization (1976).
- **24.** Lundquist, K. A., Chow, F. K. & Lundquist, J. K. An immersed boundary method for the weather research and forecasting model. *Monthly Weather Review* **138**, 796–817, https://doi.org/10.1175/2009MWR2990.1 (2010).
- **25.** Danielson, J. J. & Gesch, D. B. Global multi-resolution terrain elevation data 2010 (gmted2010). Tech. Rep. (2011). 10.3133/ofr20111073. Report.
- 26. Survey, U. U. S. G. Usgs eros archive-digital elevation-shuttle radar topography mission (srtm) 1 arc-second global (2023). Accessed on October 2023.
- **27.** Friedl, M. A., Gray, J. & Sulla-Menashe, D. Mcd12q2 modis/terra+aqua land cover dynamics yearly 13 global 500m sin grid version 6, 10.5067/MODIS/MCD12Q2.006 (2019). Accessed on 2025-06-04.
- **28.** Souza, C. M. *et al.* Reconstructing three decades of land use and land cover changes in brazilian biomes with landsat archive and earth engine. *Remote Sensing* **12**, 10.3390/rs12172735 (2020).
- **29.** Iacono, M. J. *et al.* Radiative forcing by long-lived greenhouse gases: Calculations with the aer radiative transfer models. *Journal of Geophysical Research: Atmospheres* **113**, https://doi.org/10.1029/2008JD009944 (2008). https://agupubs.onlinelibrary.wiley.com/doi/pdf/10.1029/2008JD009944.
- **30.** Zheng, Y., Alapaty, K., Herwehe, J. A., Genio, A. D. D. & Niyogi, D. Improving high-resolution weather forecasts using the weather research and forecasting (wrf) model with an updated kain-fritsch scheme. *Monthly Weather Review* **144**, 833 860, https://doi.org/10.1175/MWR-D-15-0005.1 (2016).
- **31.** Morrison, H., Thompson, G. & Tatarskii, V. Impact of cloud microphysics on the development of trailing stratiform precipitation in a simulated squall line: Comparison of one- and two-moment schemes. *Monthly Weather Review* **137**, 991 1007, https://doi.org/10.1175/2008MWR2556.1 (2009).

- **32.** Jiménez, P. A. *et al.* A revised scheme for the wrf surface layer formulation. *Monthly Weather Review* **140**, 898 918, https://doi.org/10.1175/MWR-D-11-00056.1 (2012).
- **33.** Niu, G.-Y. *et al.* The community noah land surface model with multiparameterization options (noah-mp): 1. model description and evaluation with local-scale measurements. *Journal of Geophysical Research: Atmospheres* **116**, https://doi.org/10.1029/2010JD015139 (2011). https://agupubs.onlinelibrary.wiley.com/doi/pdf/10.1029/2010JD015139.
- **34.** Hong, S.-Y., Noh, Y. & Dudhia, J. A new vertical diffusion package with an explicit treatment of entrainment processes. *Monthly Weather Review* **134**, 2318 2341, https://doi.org/10.1175/MWR3199.1 (2006).
- **35.** Dragaud, I. C. D. V. *Análise dos mecanismos físicos que governam o escoamento atmosférico na região costeira do estado do Rio de Janeiro*. Ph.D. thesis, Universidade Federal do Rio de Janeiro (2021).
- **36.** Soares da Silva, M. *et al.* Assessment of meteorological settings on air quality modeling system-a proposal for un-sdg and regulatory studies in non-homogeneous regions in brazil. *Environmental Science and Pollution Research* **30**, 1737–1760, 10.1007/s11356-022-22146-1 (2023).
- **37.** de Souza, L. S. *et al.* Evaluation of cumulus and microphysical parameterization schemes of the wrf model for precipitation prediction in the paraíba do sul river basin, southeastern brazil. *Pure and Applied Geophysics* **181**, 679–700, 10.1007/s00024-023-03419-3 (2024).
- **38.** Pedruzzi, R. *et al.* Update of land use/land cover and soil texture for brazil: Impact on wrf modeling results over paraíba do sul river basin, são paulo. *Atmospheric Environment* **268**, 118760, https://doi.org/10.1016/j.atmosenv.2021.118760 (2022).
- **39.** Jacinto, L. d. F. R. *Sistema Integrado de Modelagem Ambiental dos Fenômenos de Transporte na Área de Influência de Centrais Nucleares*. Master's thesis, Programa de Pós-Graduação em Meteorologia, PPGM, Universidade Federal do Rio de Janeiro (2020).
- **40.** Shchepetkin, A. F. & McWilliams, J. C. The regional oceanic modeling system (roms): a split-explicit, free-surface, topography-following-coordinate oceanic model. *Ocean Modelling* **9**, 347–404 (2005).
- **41.** MacFerrin, M., Amante, C., Carignan, K., Love, M. & Lim, E. The earth topography 2022 (etopo 2022) global dem dataset. *Earth System Science Data* **17**, 1835–1849, 10.5194/essd-17-1835-2025 (2025).
- **42.** Hersbach, H. *et al.* Era5 hourly data on single levels from 1940 to present, copernicus climate change service (c3s) climate data store (cds) [data set] (2023).
- **43.** Jean-Michel, L. *et al.* The copernicus global 1/12Âř oceanic and sea ice glorys12 reanalysis. *Frontiers in Earth Science* **9**, 10.3389/feart.2021.698876 (2021).
- **44.** Egbert, G. D., Bennett, A. F. & Foreman, M. G. G. Topex/poseidon tides estimated using a global inverse model. *Journal of Geophysical Research: Oceans* **99**, 24821–24852, 10.1029/94JC01894 (1994).
- **45.** Egbert, G. D. & Erofeeva, S. Y. Efficient inverse modeling of barotropic ocean tides. *Journal of Atmospheric and Oceanic Technology* **19**, 183–204 (2002).
- **46.** Good, S. *et al.* The current configuration of the ostia system for operational production of foundation sea surface temperature and ice concentration analyses. *Remote Sensing* **12**, 10.3390/rs12040720 (2020).
- 47. Telea, A. An image inpainting technique based on the fast marching method. *Journal of Graphics Tools* 9, 23–34 (2004).
- **48.** Bertalmio, M., Bertozzi, A. L. & Sapiro, G. Navier-stokes, fluid dynamics, and image and video inpainting. In *Proceedings* of the 2001 IEEE Computer Society Conference on Computer Vision and Pattern Recognition (CVPR), vol. 1, I–I (IEEE, 2001).
- **49.** Hersbach, H. Cmod5-an improved geophysical model function for ers c-band scatterometry. Tech. Rep. Tech. Memo. 395, ECMWF (2003).
- **50.** Wackerman, C. C., Pichel, W. G. & Clemente-Colon, P. Automated estimation of wind vectors from sar. In *Proceedings of the 12th Conference on Interactions of the Sea and Atmosphere* (2003).
- **51.** Bilgili, M., Alphan, H. & Ilhan, A. Potential visibility, growth, and technological innovation in offshore wind turbines installed in europe. *Environmental Science and Pollution Research* **30**, 27208–27226 (2023).

- 52. Emeis, S. Wind energy meteorology: atmospheric physics for wind power generation (Springer, 2018).
- **53.** Murphy, K. P. *Machine learning: a probabilistic perspective* (MIT Press, 2012).

## **Acknowledgements**

The authors would like to thank TotalEnergies for providing financial support for this project. We would also like to thank the Conselho Nacional de Desenvolvimento Científico e Tecnológico (CNPq) and Coordenação de Aperfeiçoamento de Pessoal de Nível Superior (CAPES) for providing scholarships to the authors.

#### Author contributions statement

Conceptualization: All authors. Methodology: All authors. Data Curation: Lívia Sancho; Mauricio S. Silva; Elisa Passos; Larissa F. R. Jacinto; Rebeca S. Lyra; Nilton O. Moraes; Carina S. Bock; Douglas M. Nehme; Raquel Toste; Carlos H. Beisl; Patrícia M. Silva; Adriano O. Vasconcelos; Rian C. Ferreira. Visualization: Luan C. V. Silva; Patricia M. Silva; Larissa F. R. Jacinto; Lívia Sancho; Mauricio S. Silva; Elisa Passos; Adriano O. Vasconcelos. Writing – Original Draft Preparation: Lívia Sancho; Mauricio S. Silva; Elisa Passos; Luan C. V. Silva; Larissa F. R. Jacinto; Raquel Toste. Validation: Luan C. V. Silva; Rodrigo S. Luna; Mauricio S. Silva; Lívia Sancho; Elisa Passos; Jacques Honigbaum; Fernando A. Rochinha; Alvaro L. G. A. Coutinho; Alexandre G. Evsukoff. Writing – Review & Editing: Luan C. V. Silva; Mauricio S. Silva; Lívia Sancho; Elisa Passos; Alexandre G. Evsukoff; Luiz P. F. Assad. Supervision: Fernando A. Rochinha; Luiz P. F. Assad; Alvaro L. G. A. Coutinho; Laura Bahiense; Alexandre G. Evsukoff. All authors reviewed and approved the final manuscript.

# **Competing interests**

The authors declare no competing interests.